ACS APPLIED MATERIALS & INTERFACES

www.acsami.org

Research Article

Normal Load and Counter Body Size Influence the Initiation of Microstructural Discontinuities in Copper during Sliding

F. Ruebeling, Y. Xu,* G. Richter, D. Dini, P. Gumbsch, and C. Greiner*

Cite This: *ACS Appl. Mater. Interfaces* 2021, 13, 4750–4760

Read Online

ACCESS | Metrics & More | Article Recommendations | Supporting Information

ABSTRACT: Near the interface of two contacting metallic bodies in relative motion, the microstructure changes. This modified microstructure leads to changes in material properties and thereby influences the tribological behavior of the entire contact. Tribological properties such as the friction coefficient and wear rate are controlled by the microstructure, while the elementary mechanisms for microstructural changes are not sufficiently understood. In this paper, the influence of the normal load and the size of the counter body on the initiation of a tribologically induced microstructure in copper after a single sliding pass is revealed. A systematic variation in the normal load and sphere diameter resulted in maximum Hertzian contact pressures between 530 MPa and 1953 MPa. Scanning electron microscopy, focused ion beam, and transmission electron microscopy were used to probe the subsurface deformation. Irrespective of the normal load and the sphere diameter, a sharp line-like feature consisting of dislocations, the so-called dislocation trace line, was identified in the subsurface area at depths between 100 nm and 400 nm. For normal loads below 6.75 N, dislocation features are formed below this line. For higher normal loads, the microstructure evolution directly underneath the surface is mainly confined to the area between the sample surface and the dislocation trace line, which itself is located at increasing depth. Transmission Kikuchi diffraction and transmission electron microscopy demonstrate that the misorientation is predominantly concentrated at the dislocation trace line. The results disclose a material rotation around axes roughly parallel to the transverse direction. This study demonstrates the generality of the trace line phenomena over a wide range of loads and contact pressures and the complexity of subsurface processes under a sliding contact and provides the basis for modeling the early stages in the microstructure evolution.

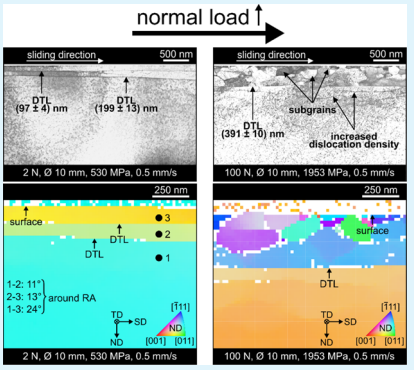

KEYWORDS: *microstructure, copper, sapphire, tribology, electron microscopy, lattice rotation*

1. INTRODUCTION

Friction, wear, and lubrication play a crucial role in our economy[1] and our standard of living depends on reliable moving systems such as gears, couplings, and clutches.[2] However, machine breakdowns are often associated with the failure of exactly these components. This calls for a better scientific understanding of tribological contacts. In the subsurface area of a sliding interface, local deformation leads to microstructural changes.[3−8] The modified material can be structurally and chemically different from the bulk.[3,9−11] These microstructural changes are associated with variations in the properties of the material and thereby affect the tribological behavior, that is, the friction coefficient (μ) and wear rate.[12−16] This implies that tribological properties can be tailored by controlling the microstructure.[17] Therefore, the elementary mechanisms for this microstructure evolution have to be known. However, these processes are not sufficiently understood[13,18−21] and most of the literature focuses on later stages in the lifetime of the contact.[13,15,22]

In previously performed dry sliding experiments between a copper plate and a sapphire sphere,[22−24] a sharp line was reported at a uniform mean depth of approximately 150 nm underneath the sample surface,[24] which was found to consist of a narrow band of dislocations. The line itself has a width of 5 to 8 nm, as reported earlier.[23] This feature was named as the dislocation trace line (DTL) and is thought to be the primer for further changes within the microstructure.[23] As this surprising feature requires a lot more attention, the present work focuses on studying a wider range of normal loads (1−100 N) and different sphere diameters (1−10 mm). All tests consisted of just one single sliding pass. Then, we followed two tracks: First, the maximum Hertzian contact pressure (p_{Hertz}) was changed from 530 to 1953 MPa by varying the normal load (2−100 N) and keeping the sphere diameter constant (10 mm); second, the influence of the sphere diameter on the microstructure evolution was systematically investigated by varying the diameter between 1 and 10 mm and the normal

Received: November 4, 2020
Accepted: December 21, 2020
Published: January 14, 2021

https://dx.doi.org/10.1021/acsami.0c19736
ACS Appl. Mater. Interfaces 2021, 13, 4750−4760

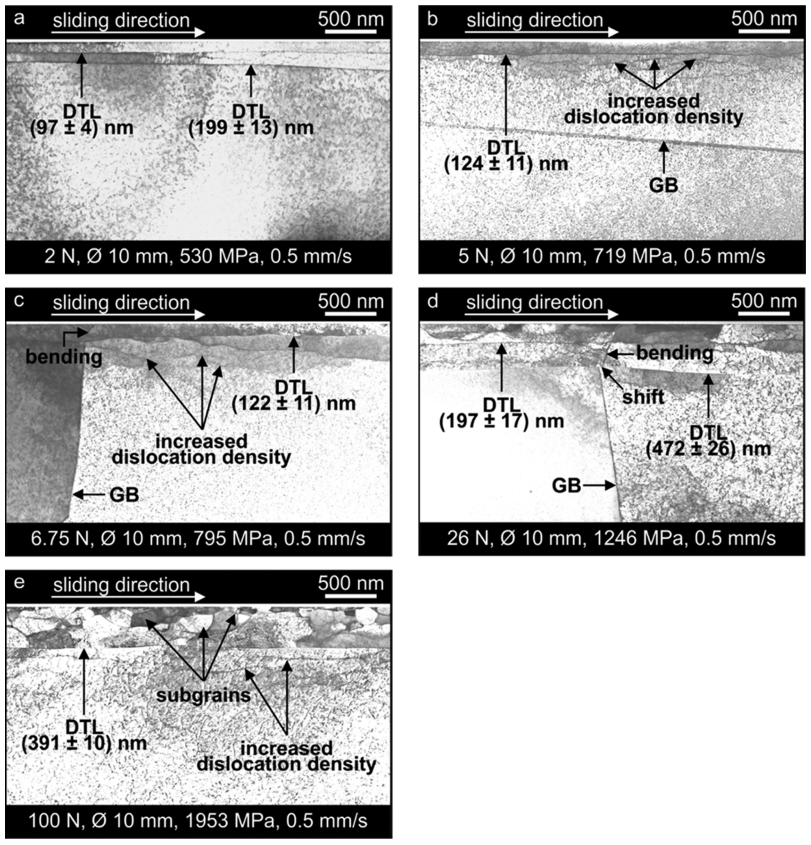

Figure 1. STEM images of the microstructure of OFHC copper after a single sliding pass for a constant sphere diameter of 10 mm and different normal loads, that is, Hertzian contact pressures. (a) F_n = 2 N (p_{Hertz} = 530 MPa), (b) F_n = 5 N (p_{Hertz} = 719 MPa), (c) F_n = 6.75 N (p_{Hertz} = 795 MPa), (d) F_n = 26 N (p_{Hertz} = 1246 MPa), and (e) F_n = 100 N (p_{Hertz} = 1953 MPa). The TEM foils were cut out of the center of the wear tracks, perpendicular to the sliding surface and parallel to the SD. The bright layer on the top of each image is the first protective platinum layer.

load (1−100 N) at a constant maximum Hertzian contact pressure of 1953 MPa.

The aim of these experiments was to study both the microstructure evolution directly underneath the surface and the characteristics of the DTL in the initial stages of a tribological contact as a function of the normal load and the size of the counter body (sphere diameter). The results are expected to guide future experimental and modeling research into the initiation of microstructural discontinuities in metals under a tribological load. In this context, our companion paper[25] employed a discrete dislocation plasticity framework to simulate the microstructure evolution underneath the surface and the activity of individual dislocations.

2. METHODS

Oxygen-free high conductivity (OFHC) copper plates (Goodfellow, Bad Nauheim, Germany) with a purity higher than 99.95% and a hardness of 58 HV 0.01/20 were used. The latter was measured with a Vickers hardness tester (Fischerscope H100, Helmut Fischer GmbH, Sindelfingen, Germany). As detailed in a previous publication,[24] any plastic deformation caused by fabrication was removed by annealing for 2 h at 500 °C (average heating-up rate 300 K/h) under vacuum and furnace cooling (average rate 80 K/h). During the annealing process, the vacuum inside the tube was better than 10^{-6} mbar. The copper plates were ground with P800, P1200, P2500, and P4000 grit SiC polishing papers (Struers, Willich, Germany) followed by cleaning in an ultrasonic bath in isopropanol for 10 min. Subsequently, the samples were polished, using a 3 and 1 μm diamond suspension (Cloeren Technology GmbH, Wegberg, Germany). Before polishing with 1 μm diamond suspension, the specimens were ultrasonically cleaned in isopropanol for 10 min. Finally, the OFHC copper plates were electropolished, using D2 electrolyte (Struers, Willich, Germany), and cleaned ultrasonically in isopropanol for 20 min. This sample preparation process led to an average areal surface roughness of 80 nm (measured using an optical 3D profiler) and an average grain size of (14 ± 1.5) μm, as determined by the line intersect method.

The reciprocating tribometer used for the tribological tests was previously described in refs 23, 24. Sapphire spheres (Saphirwerk, Brügg, Switzerland) were used as counter bodies. The average areal surface roughness of the sapphire sphere was measured using an atomic force microscope (Park XE 7, Park Systems, Suwon, Korea) to be smaller than 5 nm.

A maximum Hertzian contact pressure[26] between 530 and 1953 MPa was achieved in the first series of experiments by varying the normal load F_n (2 N, 5 N, 6.75 N, 26 N, and 100 N) and keeping the sphere diameter (d_{sphere}) constant (10 mm). Although Hertzian theory is only valid for a purely elastic contact, it is used to estimate the contact pressures. The maximum Hertzian contact pressures were calculated with Young's modulus of 117 GPa[27] and a Poisson ratio of 0.34[28] for copper. For sapphire, Young's modulus of 345 GPa[29] and a Poisson ratio of 0.3[29] were used. For the second series of experiments, the influence of the sphere diameter on the microstructure evolution right underneath the surface was systematically investigated. A normal load of 1 N, 2.25 N, 25 N, and 100 N and a corresponding sphere diameter of 1 mm, 1.5 mm, 5 mm, and 10 mm were chosen to keep the resulting maximum Hertzian contact pressure constant at 1953 MPa. Single-sliding pass experiments were performed to investigate the early stages of the microstructure evolution. The sliding speed was kept constant at 0.5 mm/s in order to be compatible with previous studies.[22,23] All tests were conducted without lubrication for a stroke length of at least 12 mm. Each experiment was performed with a new

https://dx.doi.org/10.1021/acsami.0c19736
ACS Appl. Mater. Interfaces 2021, 13, 4750−4760

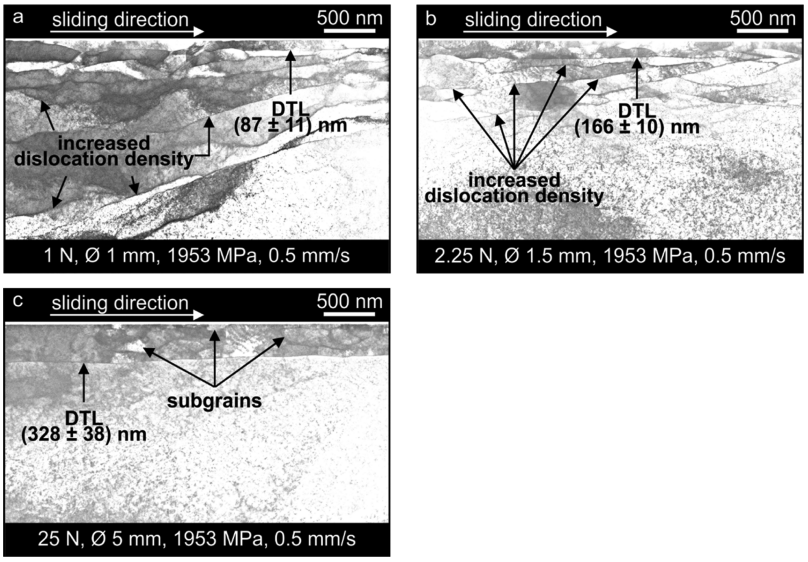

Figure 2. STEM images of the microstructure of OFHC copper after a single sliding pass for a constant Hertzian contact pressure of 1953 MPa and different normal loads and sphere diameters. (a) F_n = 1 N, d_{sphere} = 1 mm, (b) F_n = 2.25 N, d_{sphere} = 1.5 mm, and (c) F_n = 25 N, d_{sphere} = 5 mm. The specimen orientation and contrast features like those described in Figure 1.

sapphire sphere at a different, unloaded area of the copper surface. The normal load and the friction force were measured with a three-axis force sensor (Kistler, Sindelfingen, Germany). Thus, the mean friction coefficient of each sliding test was determined by dividing all the measured friction forces by the specific dead weight and calculating the mean value. The tribometer was housed in a glove box to achieve constant humidity. The sliding tests were performed in air at room temperature and a relative humidity of (50 ± 2) %.

Focused ion beam and scanning electron dual-beam microscopy (FIB/SEM) (Helios NanoLab DualBeam 650, FEI, Hillsboro, Oregon, USA) were employed to prepare site-specific transmission electron microscopy (TEM) foils from the wear tracks and probe the subsurface microstructure. The sample surface was protected from ion beam damage by depositing two platinum layers, the first one with the electron beam. TEM foils were cut out of the center of the wear tracks, perpendicular to the sliding surface and parallel to the sliding direction (SD). The foil preparation followed the procedure by Mayer et al.[30] Scanning transmission electron microscopy (STEM) images were taken at an acceleration voltage of 30 kV and a beam current of 100 pA inside the focused ion beam and scanning electron dual-beam microscope.

Transmission Kikuchi diffraction (TKD) was performed in the cross-sectional subsurface area of each TEM foil to determine the local crystallographic orientation. The area for this analysis was 1.3 μm × 1 μm, the step size was 20 nm, the acceleration voltage was 30 kV, and the beam current was 6.4 nA. The patterns were acquired with a Nordlys Max^2 detector and indexed with AZtecHKL software, both from Oxford Instruments (Oxfordshire, U.K.). The color-coded inverse pole figure for each map indicates the selected direction and thereby reveals the crystallographic orientation.

The misorientation between the area above and below the DTL determined by TKD was additionally measured by TEM. A Philips CM 200 transmission electron microscope was employed. The acceleration voltage was 200 kV. At the beginning of each TEM measurement, the area toward the bulk was tilted and rotated into low-indexed zone axes. Routinely, the tilting toward the normal of the TEM foil was smaller than 10°, such that the zone axis was nearly perpendicular to the cross-sectional view of the wear track and thereby close to the transverse direction (TD). Selected area diffraction (SAD) patterns from the bulk part of the foils and the near-surface material were acquired in order to analyze if their crystallographic orientation is different. The corresponding misorientation was determined by measuring the angle between the individual diffraction spots in the SAD patterns.

3. RESULTS

In what follows, line-like dislocation features expanding nearly parallel to the sample surface and separating regions of different crystallographic orientations are designated as DTLs. Figure 1 displays STEM images for the tribologically induced subsurface microstructures after single passes for different maximum Hertzian contact pressures and a constant sphere diameter. The bright layer on the top of these images is the first protective platinum layer. In all cases, the SD was from left to right as indicated by a white arrow.

At a depth between 100 and 400 nm, one or two DTLs are visible. For a normal load of 2 N (p_{Hertz} = 530 MPa), in Figure 1a, two line-like features are observed. The upper DTL has a mean depth of (97 ± 4) nm. The mean depth of the lower one is (199 ± 13) nm. The mean depth of each DTL was determined by measuring the depth of the DTL under the surface for at least six different positions and calculating its mean value including the standard deviation. Figure 1b displays the tribologically induced microstructure for a normal load of 5 N (p_{Hertz} = 719 MPa). A grain boundary (marked as GB) is crossing the entire image. A sharp DTL is observed at a mean depth of (124 ± 11) nm. Below this line, there are wave-like lines of darker contrast, marked by arrows, and designated as increased dislocation density. The subsurface microstructure for a normal load of 6.75 N (p_{Hertz} = 795 MPa) is shown in Figure 1c. A GB separates the microstructure almost vertically into two grains. A DTL is found at a mean depth of (122 ± 11) nm. Above the DTL, the GB bends in the direction of sliding, as indicated by an arrow. Figure 1d displays the microstructure for a normal load of 26 N (p_{Hertz} = 1246 MPa) and corresponds to the microstructure already published in Haug et al.[22] In the middle of the image, a GB separates the microstructure into two grains. Two DTLs are visible. The lower one has a mean depth of (472 ± 26) nm and is not significantly disturbed by the GB. Within the left grain, the upper DTL has a mean depth of (197 ± 17) nm. The upper DTL is wavy and less well found within the right grain. Above the lower DTL, the GB is shifted and bent in the direction of sliding, as indicated by arrows. The microstructure for a

https://dx.doi.org/10.1021/acsami.0c19736
ACS Appl. Mater. Interfaces 2021, 13, 4750−4760

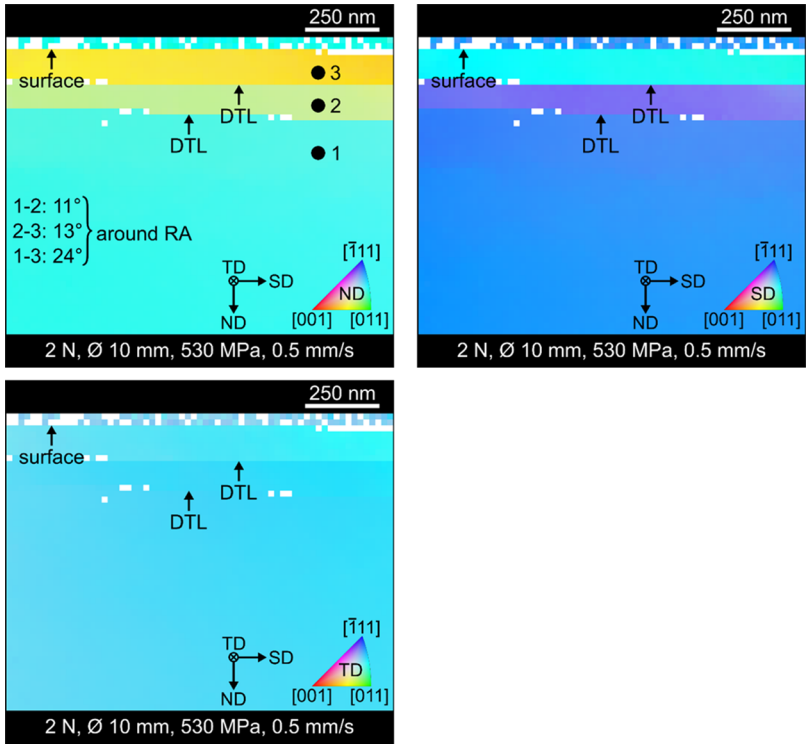

Figure 3. TKD maps in the ND, SD, and TD from the specimen for F_n = 2 N, d_{sphere} = 10 mm (p_{Hertz} = 530 MPa). Both of the DTLs are associated with a misorientation. The given misorientations within the ND map refer to the RA.

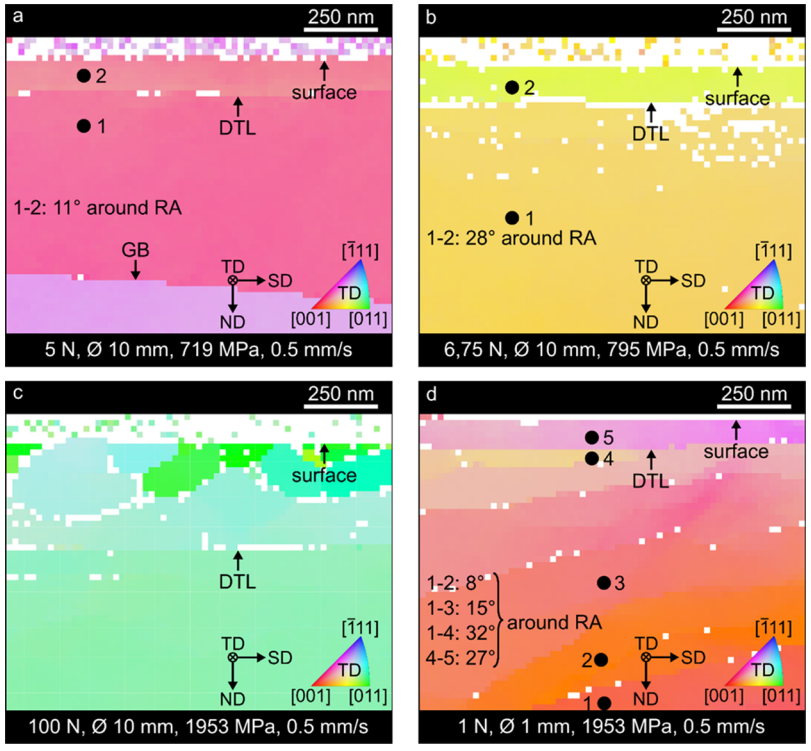

Figure 4. TKD maps in the TD and misorientations around the RA for different loading scenarios. (a) F_n = 5 N, d_{sphere} = 10 mm (p_{Hertz} = 719 MPa), (b) F_n = 6.75 N, d_{sphere} = 10 mm (p_{Hertz} = 795 MPa), (c) F_n = 100 N, d_{sphere} = 10 mm (p_{Hertz} = 1953 MPa), and (d) F_n = 1 N, d_{sphere} = 1 mm (p_{Hertz} = 1953 MPa). The given misorientations within the TD map refer to the RA. All major misorientations are concentrated at the DTL and to a lesser extent at the subgrain boundaries. The maps reveal a weak color change. (a,b) Misorientation directly above and below the DTL increases with increasing normal loads. (d) With respect to the bulk material (point 1), the lattice rotation increases incrementally with decreasing distance to the surface.

https://dx.doi.org/10.1021/acsami.0c19736
ACS Appl. Mater. Interfaces 2021, 13, 4750−4760

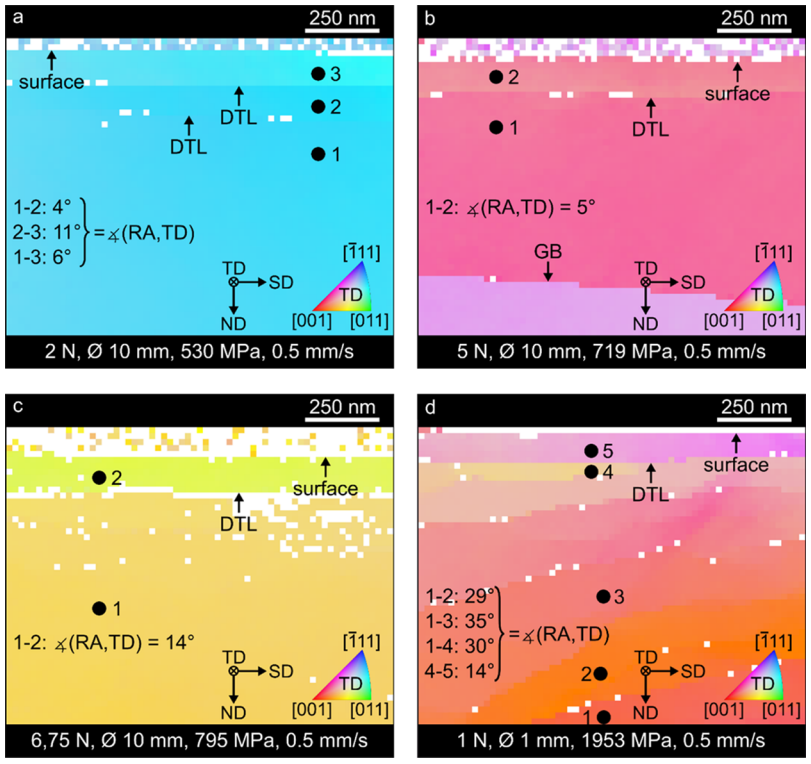

Figure 5. TKD maps in the TD and the deviation between the RA and the TD axis for different loading scenarios. (a) F_n = 2 N, d_{sphere} = 10 mm (p_{Hertz} = 530 MPa), (b) F_n = 5 N, d_{sphere} = 10 mm (p_{Hertz} = 719 MPa), (c) F_n = 6.75 N, d_{sphere} = 10 mm (p_{Hertz} = 795 MPa), and (d) F_n = 1 N, d_{sphere} = 1 mm (p_{Hertz} = 1953 MPa). The given angles within the TD map refer to the deviation of the rotation axes to the TD axis. For 2 N, 5 N, and 6.75 N, the deviation is between 4 and 14°, whereas for 1 N, the smallest deviation is right underneath the sample surface (point 4 to 5).

normal load of 100 N (p_{Hertz} = 1953 MPa) is shown in Figure 1e. This image demonstrates two characteristic zones, separated by the DTL at a mean depth of (391 ± 10) nm. Subgrains are observed between the sample surface and the DTL.

The results for single-sliding pass experiments performed with a nominally constant Hertzian contact pressure but varying sphere diameters and normal loads are presented in Figure 2.

For a sphere diameter of 1 mm and a normal load of 1 N, the microstructure in Figure 2a displays a DTL at a mean depth of (87 ± 11) nm. Further into the bulk, there are many blurred and irregular distributed lines of darker contrast, which are indicated by arrows and referred to as regions of increased dislocation density. Figure 2b displays the STEM image for a sphere diameter of 1.5 mm and a normal load of 2.25 N. At a mean depth of (166 ± 10) nm, a DTL is visible. Below this line, several sharp and connected dislocation features expand across the entire cross-section, forming a layered dislocation structure. For a sphere diameter of 5 mm and a normal load of 25 N, the deformation caused by tribological loading is shown in Figure 2c. There is one DTL visible at a uniform mean depth of (328 ± 38) nm. Some subgrains have formed within the area between the surface and the DTL. The resulting microstructure for a sphere diameter of 10 mm and a normal load of 100 N is shown in Figure 1e and has already been described there.

Figure 3 displays the subsurface crystallographic orientation determined by TKD for a normal load of 2 N and a sphere diameter of 10 mm. The maps for the normal direction (ND) and SD show a clear change in the crystallographic orientation above and below each of the DTLs. The misorientations between specific point pairs within the ND map do not refer to the axis in the ND but to the rotation axis (RA). Because of distinct differences in the orientation within the ND map, the positions of the selected points are clearly visible; therefore, this map was selected to indicate the misorientations around the RA. Two points, one below the DTL and the other above the DTL, were selected to analyze the misorientation around the RA. This angle, which is required in order to convert the orientation of these two points, was determined using custom MATLAB scripts employing the open-source toolbox MTEX.[31] The misorientation around the RA between point 1 and 2 is about 11°, whereas it is approximately 13° between point 2 and 3. This results in a total misorientation around the RA between the bulk material (point 1) and the area directly below the surface (point 3) of nearly 24°. In the TD, both DTLs are associated with a smooth contrast change, which may imply a material rotation around axes nearly parallel to the TD. This was already reported by Greiner et al.,[24] Haug et al.,[22] Cai et al.,[32] and Heilmann et al.[33]

To further investigate this orientation change for a wider range of loading conditions, the maps in the TD are shown for different normal loads in Figure 4. Although the misorientations between single-point pairs are given within the TD map, they do not refer to the TD axis but to the RA. All the maps in Figure 4 reveal a weak color change. Comparing the misorientation around the RA directly above and below the DTL for different normal loads, the misorientation increases with increasing normal load (11° in Figure 4a and 28° in Figure 4b). For 1 N and a sphere diameter of 1 mm (see Figure 4d), the lattice rotation around the RA increases incrementally with decreasing distance to the surface.

https://dx.doi.org/10.1021/acsami.0c19736
ACS Appl. Mater. Interfaces 2021, 13, 4750−4760

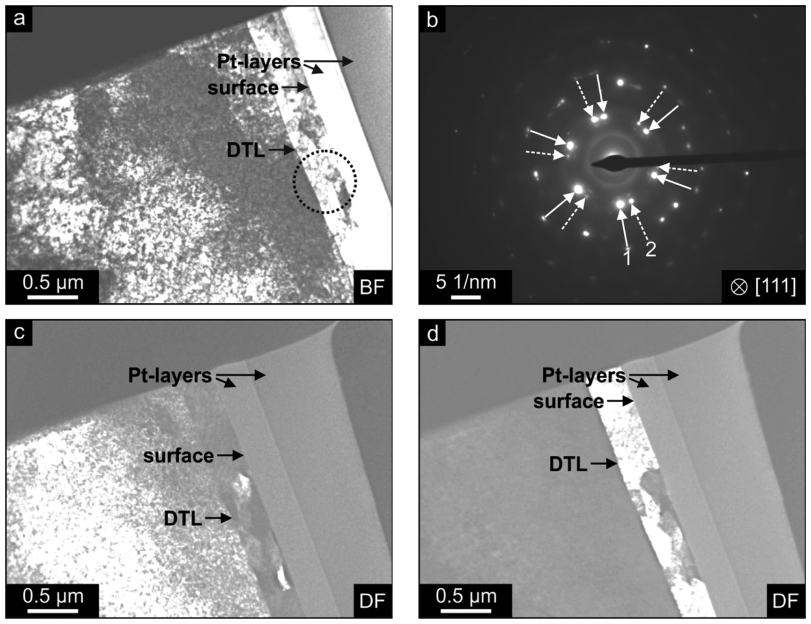

Figure 6. TEM images from the specimen for F_n = 25 N, d_{sphere} = 5 mm (p_{Hertz} = 1953 MPa). (a) BF image, (b) SAD pattern of the region marked by a dashed circle in the BF image, (c) DF image of diffraction spot 1, (d) DF image of diffraction spot 2. The continuous white arrows in (b) correspond to the main diffraction spots, whereas the secondary diffraction spots are represented by dashed white arrows. The main diffraction spots belong to the less-deformed bulk material (c), whereas the secondary diffraction spots refer to the strongly deformed microstructure right underneath the surface (d). The SAD pattern reveals a lattice rotation within the TEM foil. The zone axis for imaging was [111], which was aligned almost parallel to the TD. The first and second protective platinum layers and the sample surface and the DTL are marked by arrows.

Figure 5 reveals the deviation between the RA and the TD axis. For 2 N, 5 N, and 6.75 N, this deviation is between 4 and 14°. In Figure 5d, the smallest deviation between the RA and the TD axis among the selected pairs of points is directly underneath the surface (point 4 to 5). The corresponding maps in the ND and SD are given in the Supporting Information (Figure S1), which reveals the deviation of the RA to the ND and SD axis, respectively.

The misorientation between the area above and below the DTL as determined by TKD was also measured via TEM-based selected area diffraction. The procedure is exemplarily illustrated for the specimen already presented in Figure 2c. The results are shown in Figure 6. A bright-field (BF) image of the subsurface area is shown in Figure 6a. The SAD pattern in Figure 6b corresponds to the region marked by a dashed circle in Figure 6a. The main diffraction spots are indicated by continuous white arrows. The dark-field (DF) image in Figure 6c is obtained by choosing only diffraction spot 1 in Figure 6b for imaging. The area further into the specimen shows a bright contrast, whereas the region between the DTL and the sample surface is dark. When imaging with one of the secondary diffraction spots (diffraction spot 2 in Figure 6b), the DF image in Figure 6d is achieved. The area between the DTL and the sample surface appears bright, whereas the area below the DTL is dark. The following conclusions can be drawn: first, the SAD pattern reveals a lattice rotation within the TEM foil; second, the DF images illustrate that the misorientation is concentrated at the DTL. Very similar results are also observed in the TEM images for other loading conditions (see Figures S2–S4).

The misorientations between the area directly above and below the DTL for different normal loads as determined by TKD and TEM are summarized in Table 1. It should be emphasized that the TKD misorientations refer to the RA, whereas the misorientations determined by TEM correspond to the selected zone axis, which was aligned nearly parallel to the TD. Both measurements agree well except for the highest load of 6.75 N, where apparently TEM only detected some of the misorientations.

Table 1. Misorientations Determined by TKD and TEM for Different Normal Loads

loading conditions	misorientation by TKD (deg)	misorientation by TEM (deg)
2 N, Ø 10 mm, upper DTL	13 ± 2	13 ± 5
2 N, Ø 10 mm, lower DTL	11 ± 2	12 ± 5
5 N, Ø 10 mm	11 ± 2	10 ± 5
6.75 N, Ø 10 mm	28 ± 2	20 ± 5

4. DISCUSSION

The present work focuses on the influence of the normal load and the sphere diameter on the initiation of the tribologically induced microstructure evolution directly underneath the surface of a copper specimen after a single sliding pass of a sapphire sphere.

All measurement techniques employed here indicate significant dislocation activity underneath the surface. Irrespective of the loading conditions, a DTL is formed directly underneath the surface (see Figures 1 and 2). In rare cases, this line is wavy and rather difficult to identify (e.g., Figure 2a,b). Furthermore, in both series of experiments, a coinciding accumulation of remaining dislocations as a function of the normal load is observed. For normal loads of up to 6.75 N (see Figures 1a–c and 2a,b), regions of increased dislocation density or a second DTL is formed below the upper DTL. For normal loads higher than 6.75 N, remaining subsurface dislocations are mainly confined to the region

https://dx.doi.org/10.1021/acsami.0c19736
ACS Appl. Mater. Interfaces 2021, 13, 4750–4760

above the upper DTL (see Figures 1d,e and 2c). In the case of 100 N (see Figure 1e), subgrains dominate within this zone. It seems plausible that with increasing normal load, the shear forces acting on and right below the sample surface increase and result in a higher dislocation density and the formation of subgrains. The location where the remaining dislocations accumulate might be an indication for the movement of the dislocations, which will be discussed in the following.

According to Hamilton,[34,35] a spherical sliding indenter imposes a complex stress field underneath the surface it is moving over. In a previous publication, the formation of the DTL was explained as follows:[23] Because of the compressive stresses underneath the spherical indenter, certain dislocations are pushed into the bulk of the material at the leading edge of the contact. At the trailing edge of the contact, these dislocations then move back toward the surface. They stop moving when the critical resolved shear stress is reached. In this depth, the dislocations accumulate and form the DTL. This certainly oversimplified picture implies that the dislocations forming the DTL move from the bulk toward the surface. Considering the microstructures found for small normal loads of up to 6.75 N (see Figures 1a−c and 2a,b), this seems reasonable, particularly in Figure 2a,b, as an increased dislocation density is visible nearly across the entire STEM image. One could easily imagine dislocations moving up from the bulk piling up against those already accumulated in the DTL(s), especially as they are all expected to be of the same type and character. This is confirmed by the more detailed deterministic picture obtained using discrete dislocation plasticity in our companion paper.[25] In contrast, the microstructures for higher normal loads in Figures 1e and 2c reveal the formation of subgrains within the area between the sample surface and the DTL. For these microstructures, a piling up of dislocations moving up from the bulk is difficult to imagine. The explanation for this behavior might come back to the question where the dislocations that accumulate in the DTL originate from. Our hypothesis for the DTL's formation does not differentiate between dislocations already in the material before the tribological experiment and those generated while sliding. As was previously suggested, surface roughness sites are prime candidates for dislocation nucleation in a frictional contact.[36,37] It is therefore conceivable that dislocations from a multitude of sources—pre-existing ones and transported and multiplied during sliding and nucleated ones from the surface—are involved in the plastic response of the material as the sphere passes. Once DTLs have formed or are in the late stage of formation, the dislocations originating in the material between the uppermost DTL and the free surface pile up against the DTL—which has the effective character of a GB[22]—and self-organize in subgrain boundaries.[38,39] It stands to reason that such a process is more dominant for higher normal loads. The strong dislocation activity, which we believe is responsible for the formation of new grains between the DTL and the surface of the specimen, is also confirmed in our discrete dislocation plasticity studies[25] when the larger loads are studied (see, e.g., Figure 11 of ref 25).

The depth of maximum shear stress normalized by contact half width is 0.49 throughout the paper. At the same time, the STEM images differ significantly, as shown in Figures 1 and 2. The absolute values for the depth of the maximum shear stress according to Hertzian contact theory range from roughly 7 μm (1 mm sphere diameter and 1 N normal load) to 76 μm (10 mm sphere diameter and 100 N normal load). These values demonstrate that the maximum shear stress according to Hertz is much deeper than the features observed in the TEM foils in Figures 1 and 2. For a constant sphere diameter, the average depth of the deformed microstructure directly underneath the surface increases with the normal load (see Figure 1a,e). As expected, the plastic deformation is directly coupled with the normal load. The STEM images shown in Figure 2 clearly demonstrate that small diameters lead to more irregular dislocation structures extending deeper into the material. For a normal load of 1 N and a sphere diameter of 1 mm (see Figure 2a), the strongly deformed area directly underneath the surface expands over the entire STEM image, whereas for 25 N and a sphere diameter of 5 mm (see Figure 2c), the depth of the strongly deformed microstructure is mainly limited to the depth of the DTL. Hence, the sphere diameter has an extensive influence on the depth of the deformed microstructure directly underneath the copper surface.

For a sphere diameter of 10 mm (first set of experiments), all the mean depths of the upper DTL are plotted as a function of the normal load in Figure 7. These data can be described

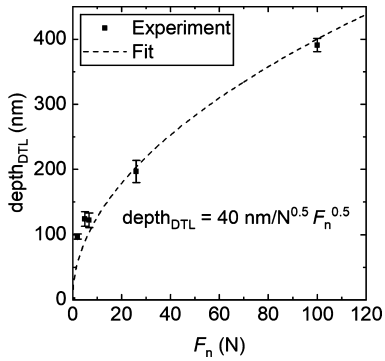

Figure 7. Depth of the upper DTL as a function of the normal load. For a sphere diameter of 10 mm, the mean depths of the upper DTL including the standard deviations are plotted as a function of the normal load. The measuring points can be fitted best (R^2 higher than 0.95) by a root function of the form $y = A \cdot x^{0.5}$, with $A \approx 40$ nm/N$^{0.5}$.

best (R^2 greater than 0.95) by a modified square root function of the form depth$_{DTL}$ = $A \cdot F_n^{0.5}$. The dashed line in Figure 7 corresponds to the fit with $A \approx 40$ nm/N$^{0.5}$. Although previous observations of the DTL reported it at essentially constant depth for the low loads applied there,[24] we find it at increasing depth for higher loads. In the literature, the growth of the tribologically altered surface layer[24] and the formation of an amorphous layer between two sliding diamond surfaces[40] were also found to follow a square root growth law.

According to Figures 3 and 4, the orientation of the grains in the TEM foils is different for all samples because they have been cut out of a polycrystal without prior crystallographic orientation determination. Nevertheless, a DTL was formed in each TEM foil. This highlights the stability of this dislocation self-organization phenomenon. All TKD patterns in the ND and SD (see Figure S1) exhibit a much more pronounced color change between the area above and below the DTL than those in the TD (see Figures 3 and 4). This implies that the material rotation during sliding is predominantly around axes roughly parallel to the TD. This is supported by determining the deviation between the RA and TD, which is shown in Figure 5. For 2 N, 5 N, and 6.75 N, this deviation is between 4 and 14°. In contrast, for these normal loads, the deviation of the RA to

https://dx.doi.org/10.1021/acsami.0c19736
ACS Appl. Mater. Interfaces 2021, 13, 4750−4760

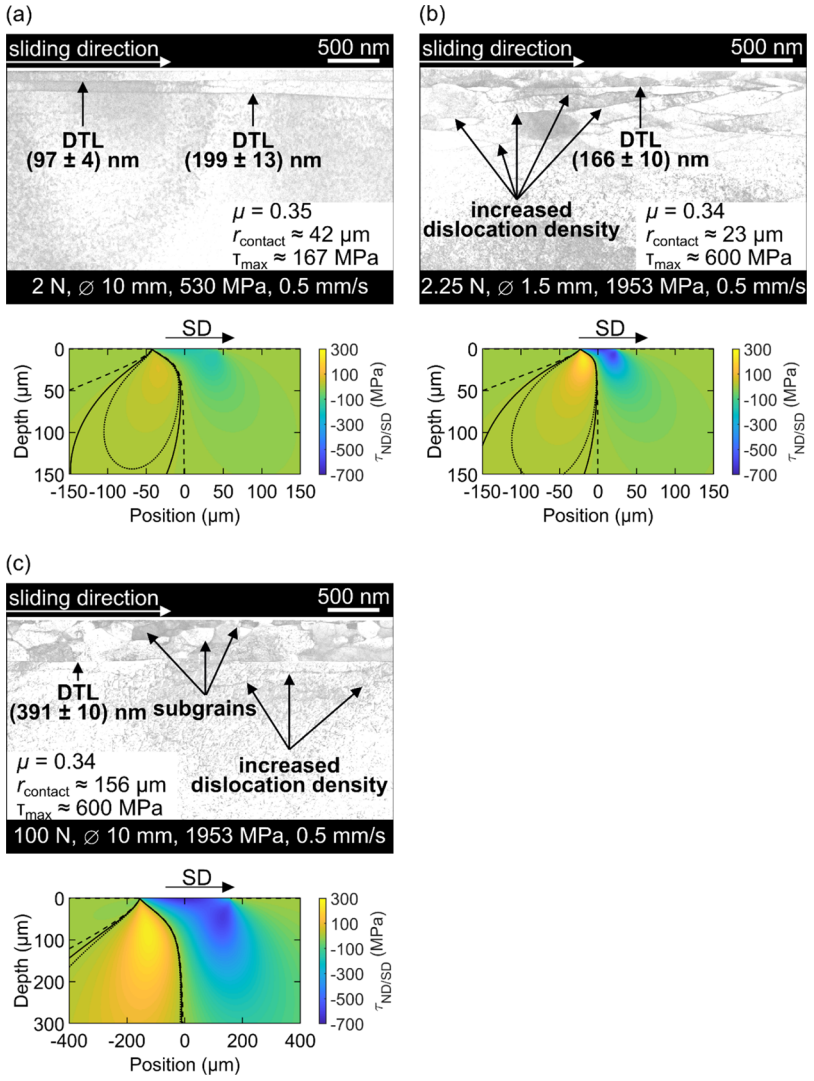

Figure 8. Influence of the sphere diameter and the normal load on the Hamilton stress field in the normal/sliding direction ($\tau_{ND/SD}$). The STEM image and the corresponding stress field (below) by Hamilton for (a) a normal load of 2 N and a sphere diameter of 10 mm, (b) a normal load of 2.25 N but a much smaller sphere diameter of 1.5 mm, and (c) a much higher normal load of 100 N and a sphere diameter of 10 mm. The shear stress components in the normal/sliding direction ($\tau_{ND/SD}$) and three isolines, 0 MPa (dashed line), 5 MPa (continuous line), and 10 MPa (dotted line), are shown. Based on the very similar progression and position of the isostress lines for constant shear stresses in (a,b), the stress fields have nearly the same size, but the contact stresses in (b) are increased compared to those in (a), and the stress field in (c) is much bigger and the contact stresses are increased.

the ND and SD axes is according to Figure S1 between 76 and 88° and therefore much larger.

The TKD data reveal a concentration of the misorientations at the DTL(s) and to a lesser extent at the subgrain boundaries. Spatially distributed and continuous crystal orientation gradients are scarcely observed. This might indicate that the energy is reduced by replacing gradients by discrete misorientation boundaries and explains why the DTL might be an energetically or kinematically favorable state. Similar considerations by Hughes and Hansen are based on such energetic arguments.[41,42]

Comparing the misorientations allows two observations: First, the lattice rotation at the DTL increases with the normal load. For a sphere diameter of 10 mm and a normal load of 2 N (see Figure 3), the misorientation is 11° (point 1 to 2), which increases up to 28° for 6.75 N (see Figure 4b). The DTL has the character of a small-angle GB for low normal loads (smaller than 6.75 N) and develops into a high-angle GB for higher normal loads. For even higher normal loads, for example, 25 N and 100 N, the misorientation between the area directly above and below the DTL cannot be determined, as there are subgrains above the DTL. Second, the misorientation with respect to the bulk material increases incrementally with decreasing distance to the surface, as can be seen in Figure 4d. Shear forces and, as a result, the number of dislocations moving on active slip systems are highest directly below the surface, leading to a maximum lattice rotation directly below the surface.

A comparison of the TKD-based misorientations with those determined by TEM shows a good agreement and a maximum deviation of 8° (see Table 1). This might be attributed to the alignment of the zone axis at the beginning of each TEM measurement, which was not exactly parallel to the RA. The inhomogeneous intensity of the diffraction spots especially in Figure S4 supports this assumption.

https://dx.doi.org/10.1021/acsami.0c19736
ACS Appl. Mater. Interfaces 2021, 13, 4750−4760

The microstructures in Figures 1 and 2 reveal a strong dependence on both the normal load and the sphere diameter. It is obvious that these parameters strongly influence the stress field under the sliding spherical indenter and that the stress field itself governs the dislocation activity and thereby the microstructure evolution.[23] This motivates us to ask whether classical contact mechanics is suitable to describe or interpret these results. Based on the abovementioned finding that the microstructure is different even for cases of nominally constant Hertzian contact pressures (see Figure 2), it is apparent that the Hertzian contact pressure is not a suitable descriptor. This is confirmed when comparing the depth of the wear track predicted by the Hertzian model with measured values. The experimental mean value of the wear track's depth is about three times higher than the Hertzian-predicted one. Hamilton extended the Hertzian picture to laterally moving contacts but also treated the contact as purely elastic.[34,35] Previously and for normal loads between 2 and 14 N, the Hamilton-based contact model was applied successfully to predict, at least in the first approximation, the depth of the DTL and to provide a qualitative description of the origin of the trace line based on dislocation activity.[23] For this reason, the Hamilton contact model is applied in the present work in order to investigate its suitability for a wide range of loading scenarios.

The stress field under a moving sphere according to Hamilton is a function of the elastic constants of the contacting materials, the Hertzian contact pressure, the contact radius ($r_{contact}$), and the friction coefficient. The materials (copper and sapphire) are kept constant, but the sphere diameter and the normal load were systematically varied. How the in-plane shear component in the normal/sliding direction ($\tau_{ND/SD}$) of the stress field—assumed to be the main driving force for dislocation motion[43]—is influenced by the Hertzian contact pressure, contact size, and friction coefficient is visualized in Figures S5−S7, respectively. These figures illustrate that the shear stress component is quite sensitive to all three parameters. In our experiments, the normal load, the sphere diameter, and the resulting friction coefficient were different in each experiment, and it is therefore illustrative to compute the stress field with the actual values of these parameters. The results are consistent with the extensive evidence provided in the literature documenting size effects in contact problems, with both the extent of the contact and the applied normal and tangential loads (which dictate the depth of the highly stressed region, the absolute level of stress, and its gradient[44]), playing a key role in determining the onset of damage and evolution of the microstructure at or in the proximity of the surface.[8,15,45−47]

Figure 8 displays the shear stress component in the ND/SD ($\tau_{ND/SD}$) and the STEM images for a variation in the sphere diameter and normal load. In Figure 8a, the sphere diameter was 10 mm and the normal load was 2 N. For a sphere diameter of 1.5 mm and a normal load of 2.25 N, the Hamilton stress field and the STEM image are shown in Figure 8b. As the normal loads are comparable in (a,b), the influence of the sphere diameter on the stress field is elucidated. The experimentally determined friction coefficients were 0.35 and 0.34 and thereby almost the same. The maximum shear stress estimated using Hamilton as shown in Figure 8a is about 170 MPa, while this is approximately 600 MPa (see Figure 8b) for the smaller sphere. It stands to reason that such a factor of 3.5 increase in shear stress will lead to a significantly higher dislocation activity and the activation of additional slip systems. This is supported by the STEM images in Figure 8a,b. For the larger sphere, we merely observe the DTL, whereas for the smaller sphere diameter, there are many horizontal dislocation features and first subgrains within the microstructure. In Figure 8c, the Hamilton stress field and the STEM image for the highest normal load of 100 N and a sphere diameter of 10 mm are shown. The higher normal load in Figure 8c compared to Figure 8a may be the reason for the increase in the dislocation activity and the formation of subgrains. Hence, the purely elastic Hamilton stress field may indicate that the generation of more complex dislocation structures, expanding deeper, can be traced back to higher shear stresses and thereby a more pronounced dislocation activity.

Modeling plasticity will allow us to better understand the origin of these features. This is performed in a companion paper by Xu et al.[25] These simulations reveal and explain the origin of the DTL using a discrete dislocation plasticity model. This is directly related to the formation of dislocation bands and the development of highly localized plasticity underneath the contact, manifesting as a thin band nearly parallel to the surface.

5. CONCLUSIONS

The microstructure evolution of OFHC copper under dry tribological loading with a sapphire sphere was systematically studied for a wide range of normal loads (1−100 N) and sphere diameters (1−10 mm). The resulting nominal Hertzian contact pressures ranged from 530 to 1953 MPa. In order to investigate the elementary mechanisms for the microstructural changes in the early stages of the sliding contact, one single sliding pass was performed. Dual-beam STEM/FIB and TEM microscopy were used to probe the subsurface deformation of the tribologically loaded samples. The key findings are summarized as follows:

- A sharp line-like feature (referred to as DTL) was observed irrespective of the normal load, the sphere diameter, and the crystallographic orientation of the initial grain, demonstrating the robustness of this dislocation self-organization phenomenon.
- For normal loads of up to 6.75 N, microstructural changes occur mainly within the area below the (upper) DTL. For normal loads higher than 6.75 N, the microstructure evolution dominates directly underneath the surface and above the (upper) DTL. For the highest normal load of 100 N, subgrains form within this zone. The DTL occurs at increasing depth with increasing load.
- Combining TKD and TEM, the DTL was found to be associated with a misorientation. The subsurface material rotates mainly around axes roughly parallel to the transverse direction.
- Keeping the sphere diameter constant, the DTL has a small-angle GB character for low normal loads (smaller than 6.75 N). It develops into a high-angle GB for higher normal loads.
- The microstructure changes although the maximum Hertzian contact pressure was kept constant. The Hamilton contact model helps to rationalize dislocation activity and the microstructure evolution directly underneath the sample surface.

https://dx.doi.org/10.1021/acsami.0c19736
ACS Appl. Mater. Interfaces 2021, 13, 4750−4760

Our study thereby demonstrates the generality of the DTL phenomenon over a large range of Hertzian contact pressures and normal loads. For higher normal loads, dislocation processes above the DTL are important, while the opposite is true for lower normal loads.

■ ASSOCIATED CONTENT

Supporting Information

The Supporting Information is available free of charge at https://pubs.acs.org/doi/10.1021/acsami.0c19736.

TKD patterns in the ND and SD and the deviations of the RA to the ND and SD axis; TEM images from the specimen for F_n = 2 N, d_{sphere} = 10 mm (p_{Hertz} = 530 MPa); TEM images from the specimen for F_n = 5 N, d_{sphere} = 10 mm (p_{Hertz} = 719 MPa); TEM images from the specimen for F_n = 6.75 N, d_{sphere} = 10 mm (p_{Hertz} = 795 MPa); influence of the Hertzian contact pressure on the Hamilton stress field beneath the sliding spherical indenter for a friction coefficient of 0.34 and a contact radius of 57.61 μm; influence of the contact radius on the Hamilton stress field beneath the sliding spherical indenter for a friction coefficient of 0.34 and a Hertzian contact pressure of 1953 MPa; and influence of the friction coefficient on the Hamilton stress field beneath the sliding spherical indenter for a Hertzian contact pressure of 1953 MPa (F_n = 2 N, d_{sphere} = 10 mm, $r_{contact}$ = 42 μm) (PDF)

■ AUTHOR INFORMATION

Corresponding Authors

C. Greiner − *Institute for Applied Materials (IAM), Karlsruhe Institute of Technology (KIT), 76131 Karlsruhe, Germany; KIT IAM-CMS MicroTribology Center (μTC), 76131 Karlsruhe, Germany;* orcid.org/0000-0001-8079-336X; Email: christian.greiner@kit.edu

Y. Xu − *Department of Materials, Imperial College London, SW7 2AZ London, U.K.; Department of Mechanical Engineering, Imperial College London, SW7 2AZ London, U.K.;* Email: yilun.xu@imperial.ac.uk

Authors

F. Ruebeling − *Institute for Applied Materials (IAM), Karlsruhe Institute of Technology (KIT), 76131 Karlsruhe, Germany; KIT IAM-CMS MicroTribology Center (μTC), 76131 Karlsruhe, Germany*

G. Richter − *Max Planck Institute for Intelligent Systems (MPI-IS), 70569 Stuttgart, Germany*

D. Dini − *Department of Mechanical Engineering, Imperial College London, SW7 2AZ London, U.K.;* orcid.org/0000-0002-5518-499X

P. Gumbsch − *Institute for Applied Materials (IAM), Karlsruhe Institute of Technology (KIT), 76131 Karlsruhe, Germany; Fraunhofer Institute for Mechanics of Materials (IWM), 79108 Freiburg, Germany*

Complete contact information is available at: https://pubs.acs.org/10.1021/acsami.0c19736

Notes

The authors declare no competing financial interest.

■ ACKNOWLEDGMENTS

C.G. acknowledges funding by the German Research Foundation (DFG) under Project G.R. 4174/1 and by the European Research Council (ERC) under Grant no. 771237, TriboKey. Y.X. and D.D. acknowledge the support of the Engineering and Physical Sciences Research Council (EPSRC) via their Established Career Fellowship EP/N025954/1. The authors thank Christian Haug for providing help with the MATLAB script for computing the stress fields.

■ REFERENCES

(1) Holmberg, K.; Erdemir, A. Influence of Tribology on Global Energy Consumption, Costs and Emissions. *Friction* **2017**, *5*, 263−284.

(2) Stachowiak, G. W.; Batchelor, A. W. *Engineering Tribology*, 3rd ed.; Elsevier Butterworth-Heinemann, 2005.

(3) Rigney, D. A.; Fu, X. Y.; Hammerberg, J. E.; Holian, B. L.; Falk, M. L. Examples of Structural Evolution during Sliding and Shear of ductile Materials. *Scr. Mater.* **2003**, *49*, 977−983.

(4) Rigney, D. A.; Naylor, M. G. S.; Divakar, R.; Ives, L. K. Low Energy Dislocation Structures Caused by Sliding and by Particle Impact. *Mater. Sci. Eng.* **1986**, *81*, 409−425.

(5) Rainforth, W. M.; Stevens, R.; Nutting, J. Deformation Structures Induced by Sliding Contact. *Philos. Mag. A* **1992**, *66*, 621−641.

(6) Emge, A.; Karthikeyan, S.; Rigney, D. A. The Effects of Sliding Velocity and Sliding Time on Nanocrystalline Tribolayer Development and Properties in Copper. *Wear* **2009**, *267*, 562−567.

(7) Hughes, D. A.; Dawson, D. B.; Korellls, J. S.; Weingarten, L. I. Near Surface Microstructures Developing under Large Sliding Loads. *J. Mater. Eng. Perform.* **1994**, *3*, 459−475.

(8) Eder, S. J.; Rodríguez Ripoll, M.; Cihak-Bayr, U.; Dini, D.; Gachot, C. Unraveling and Mapping the Mechanisms for Near-Surface Microstructure Evolution in CuNi Alloys under Sliding. *ACS Appl. Mater. Interfaces* **2020**, *12*, 32197−32208.

(9) Rigney, D. A.; Hammerberg, J. E. Unlubricated Sliding Behavior of Metals. *MRS Bull.* **1998**, *23*, 32−36.

(10) Rigney, D. A.; Karthikeyan, S. The Evolution of Tribomaterial during Sliding:A Brief Introduction. *Tribol. Lett.* **2010**, *39*, 3−7.

(11) Rigney, D. A. Transfer, Mixing and Associated Chemical and Mechanical Processes during the Sliding of Ductile Materials. *Wear* **2000**, *245*, 1−9.

(12) Perez-Unzueta, A. J.; Beynon, J. H. Microstructure and Wear Resistance of Pearlitic Rail Steels. *Wear* **1993**, *162−164*, 173−182.

(13) Emge, A.; Karthikeyan, S.; Kim, H. J.; Rigney, D. A. The Effect of Sliding Velocity on the Tribological Behavior of Copper. *Wear* **2007**, *263*, 614−618.

(14) Fischer, A.; Weiss, S.; Wimmer, M. A. The Tribological Difference between Biomedical Steels and CoCrMo-Alloys. *J. Mech. Behav. Biomed. Mater.* **2012**, *9*, 50−62.

(15) Argibay, N.; Chandross, M.; Cheng, S.; Michael, J. R. Linking Microstructural Evolution and Macro-Scale Friction Behavior in Metals. *J. Mater. Sci.* **2017**, *52*, 2780−2799.

(16) Chen, X.; Han, Z.; Li, X.; Lu, K. Lowering Coefficient of Friction in Cu Alloys with Stable Gradient Nanostructures. *Sci. Adv.* **2016**, *2*, No. e1601942.

(17) Curry, J. F.; Babuska, T. F.; Furnish, T. A.; Lu, P.; Adams, D. P.; Kustas, A. B.; Nation, B. L.; Dugger, M. T.; Chandross, M.; Clark, B. G.; Boyce, B. L.; Schuh, C. A.; Argibay, N. Achieving Ultralow Wear with Stable Nanocrystalline Metals. *Adv. Mater.* **2018**, *30*, 1802026.

(18) Rice, S. L.; Nowotny, H.; Wayne, S. F. A Survey of the Development of Subsurface Zones in the Wear of Materials. *Key Eng. Mater.* **1989**, *33*, 77−100.

(19) Greiner, C.; Gagel, J.; Gumbsch, P. Solids under Extreme Shear: Friction-Mediated Subsurface Structural Transformations. *Adv. Mater.* **2019**, *31*, 1806705.

(20) Beckmann, N.; Romero, P. A.; Linsler, D.; Dienwiebel, M.; Stolz, U.; Moseler, M.; Gumbsch, P. Origins of Folding Instabilities on Polycrystalline Metal Surfaces. *Phys. Rev. Appl.* **2014**, *2* (). DOI: DOI: 10.1103/PhysRevApplied.2.064004.
(21) Sawyer, W. G.; Argibay, N.; Burris, D. L.; Krick, B. A. Mechanistic Studies in Friction and Wear of Bulk Materials. *Annu. Rev. Mater. Res.* **2014**, *44*, 395−427.
(22) Haug, C.; Ruebeling, F.; Kashiwar, A.; Gumbsch, P.; Kübel, C.; Greiner, C. Early Deformation Mechanisms in the Shear Affected Region underneath a Copper Sliding Contact. *Nat. Commun.* **2020**, *11*, 839.
(23) Greiner, C.; Liu, Z.; Schneider, R.; Pastewka, L.; Gumbsch, P. The Origin of Surface Microstructure Evolution in Sliding Friction. *Scr. Mater.* **2018**, *153*, 63−67.
(24) Greiner, C.; Liu, Z.; Strassberger, L.; Gumbsch, P. Sequence of Stages in the Microstructure Evolution in Copper under Mild Reciprocating Tribological Loading. *ACS Appl. Mater. Interfaces* **2016**, *8*, 15809−15819.
(25) Xu, Y.; Ruebeling, F.; Balint, D. S.; Greiner, C.; Dini, D. On the Origin of Microstructural Discontinuities in Sliding Contacts: A Discrete Dislocation Plasticity Analysis. submitted to International Journal of Plasticity.
(26) Hertz, H. Über die Berührung fester elastischer Körper. *J. für die Reine Angewandte Math.* **2009**, *1882*, 156.
(27) Wang, Z.; Nian, T.; Ryding, D.; Kuzay, T. M. Low-Cycle-Fatigue Behavior of Copper Materials and their Use in Synchrotron Beamline Components. *Nucl. Instrum. Methods Phys. Res. Sect. A Accel. Spectrom. Detect. Assoc. Equip.* **1994**, *347*, 651−656.
(28) Goodfellow GmbH, http://www.goodfellow.com/de/.
(29) Pishchik, V.; Dobrovinskaya, E. R.; Lytvynov, L. A. *Sapphire: Material, Manufacturing, Applications*; Micro- and Opto-Electronic Materials, Structures, and Systems; Springer-Verlag US, 2009.
(30) Mayer, J.; Giannuzzi, L. A.; Kamino, T.; Michael, J. TEM Sample Preparation and FIB-Induced Damage. *MRS Bull.* **2007**, *32*, 400−407.
(31) Bachmann, F.; Hielscher, R.; Schaeben, H. Texture Analysis with MTEX − Free and Open Source Software Toolbox. *Solid State Phenom.* **2010**, *160*, 63−68.
(32) Cai, W.; Bellon, P.; Beaudoin, A. J. Probing the Subsurface Lattice Rotation Dynamics in Bronze after Sliding Wear. *Scr. Mater.* **2019**, *172*, 6−11.
(33) Heilmann, P.; Clark, W. A. T.; Rigney, D. A. Orientation Determination of Subsurface Cells Generated by Sliding. *Acta Metall.* **1983**, *31*, 1293−1305.
(34) Hamilton, G. M. Explicit Equations for the Stresses beneath a Sliding Spherical Contact. *Proc. IME C J. Mech. Eng. Sci.* **1983**, *197*, 53−59.
(35) Hamilton, G. M.; Goodman, L. E. The Stress Field Created by a Circular Sliding Contact. *J. Appl. Mech.* **1966**, *33*, 371.
(36) Chen, X.; Schneider, R.; Gumbsch, P.; Greiner, C. Microstructure Evolution and Deformation Mechanisms during High Rate and Cryogenic Sliding of Copper. *Acta Mater.* **2018**, *161*, 138−149.
(37) Chen, X.; Han, Z.; Lu, K. Friction and Wear Reduction in Copper with a Gradient Nano-grained Surface Layer. *ACS Appl. Mater. Interfaces* **2018**, *10*, 13829−13838.
(38) Hughes, D. A.; Hansen, N. Deformation Structures Developing on Fine Scales. *Philos. Mag.* **2003**, *83*, 3871−3893.
(39) Hughes, D. A.; Hansen, N.; Bammann, D. J. Geometrically Necessary Boundaries, Incidental Dislocation Boundaries and Geometrically Necessary Dislocations. *Scr. Mater.* **2003**, *48*, 147−153.
(40) Pastewka, L.; Moser, S.; Gumbsch, P.; Moseler, M. Anisotropic Mechanical Amorphization Drives Wear in Diamond. *Nat. Mater.* **2011**, *10*, 34−38.
(41) Hansen, N.; Kuhlmann-Wilsdorf, D. Low Energy Dislocation Structures due to Unidirectional Deformation at Low Temperatures. *Mater. Sci. Eng.* **1986**, *81*, 141−161.
(42) Kuhlmann-Wilsdorf, D. Theory of Plastic Deformation:Properties of Low Energy Dislocation Structures. *Mater. Sci. Eng., A* **1989**, *113*, 1−41.
(43) Hull, D.; Bacon, D. J. *Introduction to Dislocations*, 5th ed.; Butterworth-Heinemann: New York, N.Y., 2011.
(44) Nowell, D.; Dini, D.; Hills, D. A. Recent Developments in the Understanding of Fretting Fatigue. *Eng. Fract. Mech.* **2006**, *73*, 207−222.
(45) He, C. G.; Ding, H. H.; Shi, L. B.; Guo, J.; Meli, E.; Liu, Q. Y.; Rindi, A.; Zhou, Z. R.; Wang, W. J. On the Microstructure Evolution and Nanocrystalline Formation of Pearlitic Wheel Material in a Rolling-Sliding Contact. *Mater. Charact.* **2020**, *164*, 110333.
(46) Vakis, A. I.; Yastrebov, V. A.; Scheibert, J.; Nicola, L.; Dini, D.; Minfray, C.; Almqvist, A.; Paggi, M.; Lee, S.; Limbert, G.; Molinari, J. F.; Anciaux, G.; Aghababaei, R.; Echeverri Restrepo, S.; Papangelo, A.; Cammarata, A.; Nicolini, P.; Putignano, C.; Carbone, G.; Stupkiewicz, S.; Lengiewicz, J.; Costagliola, G.; Bosia, F.; Guarino, R.; Pugno, N. M.; Müser, M. H.; Ciavarella, M. Modeling and Simulation in Tribology across Scales: An Overview. *Tribol. Int.* **2018**, *125*, 169−199.
(47) Xu, Y.; Dini, D. Capturing the Hardness of Coating Systems across the Scales. *Surf. Coat. Technol.* **2020**, *394*, 125860.

https://dx.doi.org/10.1021/acsami.0c19736
ACS Appl. Mater. Interfaces 2021, 13, 4750−4760